



Influence of micro-segregation on the microstructure, and microhardness of MoNbTa_xTi_(1-x)W refractory high entropy alloys: Experimental and DFT approach

Shanker Kumar ^a, Albert Linda ^b, Yagnesh Shadangi ^c, Vikas Jindal ^{a,*}

^a Department of Metallurgical Engineering, Indian Institute of Technology (Banaras Hindu University), Varanasi, 221005, Uttar Pradesh, India

^b Department of Materials Science and Engineering, Indian Institute of Technology, Kanpur, 208016, Uttar Pradesh, India

^c Department of Materials Science and Engineering, Seoul National University, Seoul, 08826, Republic of Korea

ARTICLE INFO

Keywords:

Refractory high entropy alloy
MoNbTaTiW
Microstructure
Indentation behavior
First principle calculations
Special quasi random structure

ABSTRACT

In recent times, MoNbTaW Refractory High Entropy Alloys (RHEAs) have drawn attention due to their exciting high-temperature applications and efforts are being made to improve their properties further. Alloying addition is an effective and practical approach to enhancing material properties. Ti is well known for its strength, low density, and corrosion resistance and its role in the properties of MoNbTaW-based RHEAs is required to be understood. RHEAs are commonly synthesized by vacuum arc melting (VAR) process and micro-segregation of the elements is reported. However, the effect of micro-segregation on MoNbTaW RHEAs is not well understood. Hence, the present work deals with the addition of Ti and micro-segregation on the structure, microstructure, and indentation behavior of MoNbTaW RHEAs. A novel non-equiautomic MoNbTa_xTi_{1-x}W ($x = 0, 1$, and 0.5) RHEAs were prepared by vacuum arc melting (VAR) process. The structure and microstructure of these RHEAs were ascertained through X-ray diffraction (XRD) and transmission electron microscopy (TEM), scanning electron microscopy (SEM) equipped with EDS for ascertaining the nominal chemical composition. The as-cast MoNbTa_xTi_{1-x}W ($x = 0, 1$, and 0.5) RHEAs contains two BCC phase having slightly different lattice parameter i.e., BCC1 ($a = 0.324$ nm) and BCC2 ($a = 0.323$ nm) close to Ti and W respectively. These as-cast RHEAs having dendritic and inter-dendritic regions were found to be enriched in W and Ta, and Mo, Nb and Ti respectively. The microhardness of these RHEAs was investigated through instrumented indentation techniques. The microhardness of the BCC1 and BCC2 phases was found to be ~ 4.5 GPa and 5.7 GPa. Further, the influence of Ti addition on the structure, elastic constant, and microhardness were estimated from the perspective of the first principle approximation. The special quasi-random structure (SQS) was used for first-principle calculations. The strengthening mechanisms influencing the mechanical properties in these BCC RHEAs were discussed in details. The experimental results were in good agreement with the results pertaining to theoretical modelling, demonstrating the effectiveness of these methods in predicting the structure and mechanical properties of RHEAs.

1. Introduction

The stringent environmental norms have enunciated the need for advanced materials with better microstructural features and mechanical properties. In most conventional alloys, solute atoms are added to the base metals in minor fractions to enhance their properties [1]. The presence of alloying elements in higher amounts usually leads to the formation of intermetallic. On the contrary to the conventional concept of alloy design, Cantor et al. [2] and Yeh et al. [3] in the year 2004 independently reported the formation of a disordered single phase in

multi-principal elements in equiautomic or near-equiautomic fractions usually referred to as high entropy alloys (HEAs). The HEAs have excellent mechanical properties, wear and corrosion resistance, and thermal stability [1]. During its initial days, most of the work on HEAs was limited to compositions containing 3d transition elements without or with the addition of Al. However, in recent times Miracle and Senkov [4] categorized various classes of HEAs such as low-density HEAs (LDHEAs), refractory elements containing HEAs (RHEAs), high entropy steel (HES), high entropy intermetallic, etc. Among the various classes of HEAs, refractory high entropy alloys (RHEAs) were found to have good

* Corresponding author.

E-mail address: vijindal@gmail.com (V. Jindal).

room temperature and high temperature strength, thermal stability, oxidation resistance, irradiation resistance, and electrical resistivity [5–8].

The RHEAs were first studied and reported in 2010 by Senkov et al. [7]. They have developed two equiatomic RHEAs having composition of MoNbTaW and MoNbTaWV through vacuum arc re-melting (VAR). These RHEAs were found to have disordered BCC structure and were found to be stable up to 1400 °C (1673 K). The MoNbTaW and MoNbTaWV RHEAs have excellent microhardness ~4.45 GPa and ~5.25 GPa respectively. Further, these RHEAs were found to have good compressive strength (~400 MPa) up to 1600 °C (1873 K). The initial work by Senkov and co-workers have surged the path for design and development of many RHEAs compositions containing refractory elements like Ti, V, Cr, Zr, Nb, Mo, Hf, Ta and W [7–10]. These RHEAs are usually synthesized by vacuum arc melting (VAR) [6], mechanical alloying (MA) [11], additive manufacturing (AM) [12], and magnetron sputtering [13] etc. Among the available techniques, VAR is most widely used for synthesis of RHEAs. A few researchers have attempted its synthesis through powder metallurgical routes. However, the high melting point and low self-diffusion co-efficient of refractory elements, and contamination during MA imposes additional challenges.

The equiatomic MoNbTaW RHEA is considered to have highest melting point (3157 K). A few compositions of MoNbTaW RHEAs having alloying addition of elements like Ti, V and Al etc. are also developed [14–17]. Li et al. [18–21] added Zr in MoNbTaW system and reported hardness of dendritic and interdendritic regions. The hardness of dendritic region is higher than interdendritic region. In an investigation, Zou et al. [22] have established the size dependent plasticity of MoNbTaW RHEAs with the help of micro-pillar compression. The strength of these RHEAs was found to be ~3.5 times higher than the bulk counterpart [23]. Kanchi et al. [24] have investigated the effect of thermo-mechanical processing on mechanical properties of MoNbTaW RHEAs. The hardness of these RHEAs was found to be ~5.68 GPa, which is ~1.5 times better than the as-cast samples. Further, they reported the segregation of elements after thermo-mechanical processing. The dendritic and inter-dendritic regions were found to be enriched in W, and Mo and Nb respectively. Similar results were also reported by Zhang et al. [25] for MoNbTaW RHEAs with alloying addition of Ti and V. The hardness of these RHEAs were found ~5.68 GPa. However for MoNbTaTiV RHEAs, the dendritic region was found to be enriched in Ta and W, and the inter-dendritic region was found to be enriched with Ti, V and Nb. The influence of Ti addition on the mechanical properties of MoNbTaW and MoNbTaWV was investigated by Han et al. [15]. They have prepared MoNbTaTiW and MoNbTaTiVW RHEAs by VAR followed by annealing at 1200 °C (1473 K) for 24 h. They reported the addition of Ti enhanced the strength along with compressive ductility. The yield strength (YS) was found to be ~586 MPa and ~659 MPa for MoNbTaTiW and MoNbTaTiVW RHEAs at 1200 °C (1473 K). Further, Han et al. [26] made attempts to investigate the effect of Ti variation in MoNbTaTi_xW ($x = 0, 0.25, 0.5, 0.75, 1.0$). They reported the formation of a single BCC structure having dendritic and inter-dendritic microstructure. The YS of these RHEAs were found to be ~1455 MPa, which is around 5 times more than the MoNbTaW RHEAs [26]. The addition of Ti has a synergistic effect on the strength and ductility. In a recent investigation Zong et al. [27] reported the high irradiation resistance for MoNbTaTi, MoNbTiW and MoNbTaTiW RHEAs. The irradiation resistance were found out to be much better than the pure W. The initial investigation on the addition of Ti in MoNbTaW type RHEAs have established the alloying addition to be more effective and practical approach for improving the mechanical properties rather than heat-treatment or thermo-mechanical processing. Therefore, it is of paramount importance to investigate the role of Ti addition in the MoNbTaW RHEAs. Further, the large disparity in the microstructure and microhardness needs to be understood in greater details. The microhardness in MoNbTaW based RHEAs were reported in a wide range ~4–13 GPa depending upon the microstructure and processing

techniques [11,12,15,26,28,29]. A recent study by Kalali et al. [11] reported the decomposition of BCC phases in MoNbTaTiW RHEA prepared by milling followed SPS in to a major BCC phase accompanied with two minor FCC phases. The structural and microstructural changes has led to a significant enhancement in the microhardness to the tune of ~13.89 GPa at 500 g load.

A few researchers and co-workers have made significant contributions in understanding the influence of RHEAs composition on the micro-segregation and its underlying influence on the microstructure and mechanical properties. Conventionally, micro-segregation phenomena depend mainly on the solidification conditions such as cooling rate, temperature gradient, casting techniques, etc. However, the micro-segregation in the case of HEAs is also dependent on factors such as melting point and self-diffusion co-efficient of constituent elements along with the solidification conditions [30–33] The RHEAs are prone to micro-segregation and their study is important. Micro-segregation in RHEAs generally leads to localized regions with different nominal compositions. These variations can potentially compromise the RHEAs mechanical properties, thermal stability, and other functional properties. It is of utmost importance to understand and mitigate the influence of micro-segregation on microstructure and mechanical properties, which are crucial for ensuring the safety and reliability of engineering components. Therefore, it is of paramount importance to understand the structure, microstructure and microhardness in these MoNbTaTiW RHEAs experimentally as well as theoretically in view of micro-segregation.

In the present investigation systematic efforts will be made to study the influence of Ti addition and micro-segregation on structure, microstructure and indentation behavior in MoNbTaW RHEAs with focus on dendritic region (DR) and inter-dendritic region (IDR), and bulk properties. The influence of replacing Ta with Ti is investigated experimentally and theoretically by first principle calculations in MoNbTa_xTi_{1-x}W ($x = 0, 1, \text{ and } 0.5$) RHEAs prepared by vacuum arc melting. To the best of our understanding this is the first systematic study to establish the presence of BCC solid solution in MoNbTa_xTi_{1-x}W ($x = 0, 1, \text{ and } 0.5$) RHEAs compositions having slightly different lattice parameter for DR and IDR. The microhardness of these two regions in RHEAs were also found to be distinct. The effect of Ti and Ta variation and micro-segregation in MoNbTaW RHEAs on the structure, microstructure and microhardness has been discussed in details in correlation with thermodynamic parameters, first principle calculations and strengthening mechanisms.

2. Experimental and computation methods

2.1. Experimental details

The metals shots of Mo, Nb, Ta, Ti and W were procured from Alfa Aesar (Thermo Fisher Corporation) having a purity of ~99.90 %. The MoNbTa_xTi_{1-x}W ($x = 0, 1, \text{ and } 0.5$) RHEA compositions were prepared using VAR in an Argon atmosphere. The Ti-getter have been placed inside the vacuum chamber so as to avoid any oxidation during melting. These RHEAs were re-melted for at least five times to attaining homogenization. Each button of these RHEAs was around ~10 g in weight. The sample designation of these three (03) RHEAS composition is mentioned in Table 1.

The RHEAs having a thickness of 3 mm were sectioned from the as-cast samples using wire-EDM cutter for structural, microstructural and indentation testing. These samples were polished using coarse emery papers for removing the wire tracks generated during cutting. The structural information of these RHEAs was ascertained through XRD and TEM. The phase analysis of as-cast samples was analyzed through Rigaku MiniFlex 600 X-ray diffractometer, operating at a voltage and current of 40 kV and 15 mA respectively. A monochromatic Cu-k_α ($\lambda = 0.15402 \text{ nm}$) used as a target material with a scan range of 20°–120°. The crystallite size and lattice strain of these RHEAs were determined

Table 1

Sample designation, phase fraction and lattice parameter of refractory high entropy alloys.

Composition	MoNbTaW		MoNbTiW		MoNbTa _{0.5} Ti _{0.5} W	
Sample designation		RHEA1		RHEA2		RHEA3
Phases		BCC1	BCC2	BCC1	BCC2	BCC1
Phase fraction (%)		70	30	75	25	83
Lattice Parameter (Å)	Experimental	3.24	3.23	3.21	3.20	3.21
	SQS	3.23		3.19		3.21

BCC1 (W-type host lattice); BCC2 (Mo-type host lattice).

through Williamson-Hall (W-H) plot [34–36]. The broadening in the samples were calculated through Pseudo-voigt fitting [37]. Further, the precise lattice parameter was obtained using the Nelson-Riley function, where the calculated lattice parameter was plotted against $(\cos^2\theta/\sin\theta + \cos^2\theta/\theta)$ [38]. For TEM analysis of these RHEAs, samples were thinned down to a thickness of $\sim 30\text{--}20\ \mu\text{m}$. A 3 mm diameter samples were punched from the thinned foil and was further subjected to twin-jet electro polishing (Struers model no TenuPol –5). For electrolytic thinning, a 5 % Perchloric acid and Methanol at a temperature of 243K with applied Voltage, 23 mV and 80 mA was used for obtaining electron transparent sample for TEM. The fine microstructural features and structural information of these RHEAs were revealed through TEM (TECNAI G²T20, FEI) at an operating voltage of 200 kV in diffraction contrast mode. The microstructural and chemical examination of these RHEAs were discerned through optical metallography and SEM-EDS analysis. For microstructural examination these samples were mechanically polished with emery paper up to ~ 2400 grit size followed by cloth polishing with alumina suspension. The optical micrograph was recorded using Leica DFC295 optical microscope. The QUANTA 200 F SEM was used for the analysis of the microstructural features in both back-scattered electron (BSE) and secondary electron (SE) modes. The chemical composition of the as-cast samples was determined through the energy-dispersive X-ray spectroscopy (EDS) detector attached to SEM. The compositional values are an average of at least five measurements, where the error is the standard deviation. The indentation behavior of these samples was observed through instrumented indentation tester (MHT³, Anton Paar) at a load of 200 mN with a dwell time of 20 s using a Vickers indenter. Efforts were made of investigate the microhardness and modulus of the dendritic and inter-dendritic regions separately.

2.2. Computation methods

The various thermodynamic and physical parameters of the RHEAs were calculated through Miedema's model [39] and density functional theory [40]. The Miedema's model have been used to estimate the enthalpy of mixing (ΔH_{mix}) for binary sub-systems in RHEAs. The regular solution model has been used to extrapolate the binary enthalpy data to predict the enthalpy of mixing for RHEAs (ΔH_{mix}) compositions. Further, efforts were made to estimate the other parameters such as entropy of mixing (ΔS_{mix}), atomic size mismatch (δ), and valence electron concentration (VEC) [41].

The thermodynamic parameters and physical properties were also estimated through first principle approximation using density functional theory. The complete disordered structure in RHEAs were generated with the help of special quasirandom structure (SQS) using the ATAT toolkit [42], which uses the monte-carlo algorithm. A conventional supercell of disordered BCC having dimension of 4x4x5 unit cells (160 atoms) was generated for each composition. With tests, we found clusters of pairs, triplets, and quadruplets each up to the third nearest neighbor were found to be sufficient for our study; hence was chosen for SQS. As SQS generation takes a fairly long amount of time, ten instances for each composition were run, and selection among them was made based on the correlation function.

Ab initio calculation was carried out using VASP [43] using the

projector augmented wave (PAW) [44] method with Perdew-Burke-Ernzerhof (PBE) functional [45]. At first, volume relaxation was carried out and a cutoff of 500 eV was used. Smearing was done using the Methfessel-Paxton scheme of order one with a smearing width of 0.1eV. The calculation was carried out using real-space projection as we have a sufficiently large number of atoms. For ionic relaxation, an energy difference of 10^{-4} eV was chosen. The K-point sampling was done using the automatic mesh generation scheme with an Rk length of 55. After obtaining the relaxed structure, the elastic constants calculations were carried out using VASPKIT [46] in the stress-strain method. Nine sets of strains, from -0.02 to $+0.02$ with an interval of 0.005, were used to generate the deformed structure. The structure was relaxed using the same parameters, except that force criterion of 10^{-2} eV/Ang was used for the present investigation.

3. Results

The phases formed in the as-cast MoNbTa_xTi_{1-x}W ($x = 0, 1$, and 0.5) RHEA compositions were discerned through XRD pattern shown in Fig. 1. The XRD pattern shown in Fig. 1 (a), 1 (b) and 1 (c) shows the presence of BCC structure in MoNbTaW, MoNbTiW and MoNbTa_{0.5}Ti_{0.5}W RHEAs respectively. The presence of BCC phase was confirmed by indexing of the planes i.e. (110), (200), (211), (220), and (310) as shown in Fig. 1(a-c). However, the closer examination of these XRD pattern indicates the presence of BCC phases having lattice parameter very close to each other as evident from the asymmetric nature of major reflection corresponding to BCC phases. The presence of BCC structures with slightly varying lattice parameters (BCC1 and BCC2) was discerned through deconvolution of the intense reflections as shown in Fig. 1 (a1-a4), 1 (b1-b4), 1 (c1-c4) for RHEA1, 2 and 3 respectively. The major diffraction peaks of BCC1 corresponds to (110) ($d \sim 2.238\ \text{\AA}$), (200) ($d \sim 1.582\ \text{\AA}$), (211) ($d \sim 1.292\ \text{\AA}$), (220) ($d \sim 1.118\ \text{\AA}$), and (310) ($d \sim 1.008\ \text{\AA}$) in RHEA 1, 2 and 3 as evident from Fig. 1 (a, a1-a4), 1 (b, b1-b4), 1 (c, c1-c4). Similarly, the major diffraction peaks of BCC2 corresponds to (110) ($d \sim 2.225\ \text{\AA}$), (200) ($d \sim 1.574\ \text{\AA}$), (211) ($d \sim 1.285\ \text{\AA}$), (220) ($d \sim 1.112\ \text{\AA}$), and (310) ($d \sim 0.995\ \text{\AA}$) in RHEA 1, 2 and 3 as evident from Fig. 1 (a, a1-a4), 1 (b, b1-b4), 1 (c, c1-c4). The precision lattice parameter of the BCC1 and BCC2 is close to that of W (cI2, $a = 3.165\ \text{\AA}$; PDF Card No.: 00-004-0806) and Mo (cI2, $a = 3.147\ \text{\AA}$; PDF Card No.: 00-004-0809). The lattice parameter of BCC1 and BCC2 are mentioned in Table 1 and is very close to each other. However, it was observed that the addition of Ti in MoNbTaW RHEAs leads to decrease in precision lattice parameter (Table 1). The phase fraction of BCC1 and BCC2 was found to be $\sim 70\%$ and 30% , $\sim 75\%$ and 25% , and $\sim 83\%$ and 17% for RHEA1, RHEA2 and RHEA3 respectively. The phase fraction of BCC1 is more than the BCC2 (Fig. 1 and Table 1).

The diffraction contrast images of MoNbTaW, MoNbTiW, and MoNbTa_{0.5}Ti_{0.5}W RHEAs are shown in Fig. 2. Fig. 2 (a), (c), and (e) represent the bright-field (BF) image of RHEA 1, 2 and 3 respectively. The BF images of the RHEAs represents the bend contour in these samples without any signature corresponding to the strain accumulation or nanostructured grains. However, the BF images shows presence of dislocation loops in the as-cast RHEAs. Fig. 2 (b), (d) and (f) represents the selected area diffraction (SAD) pattern for RHEA 1, 2 and 3 respectively. The SAD pattern of RHEA1 shown in Fig. 2 (b) represents

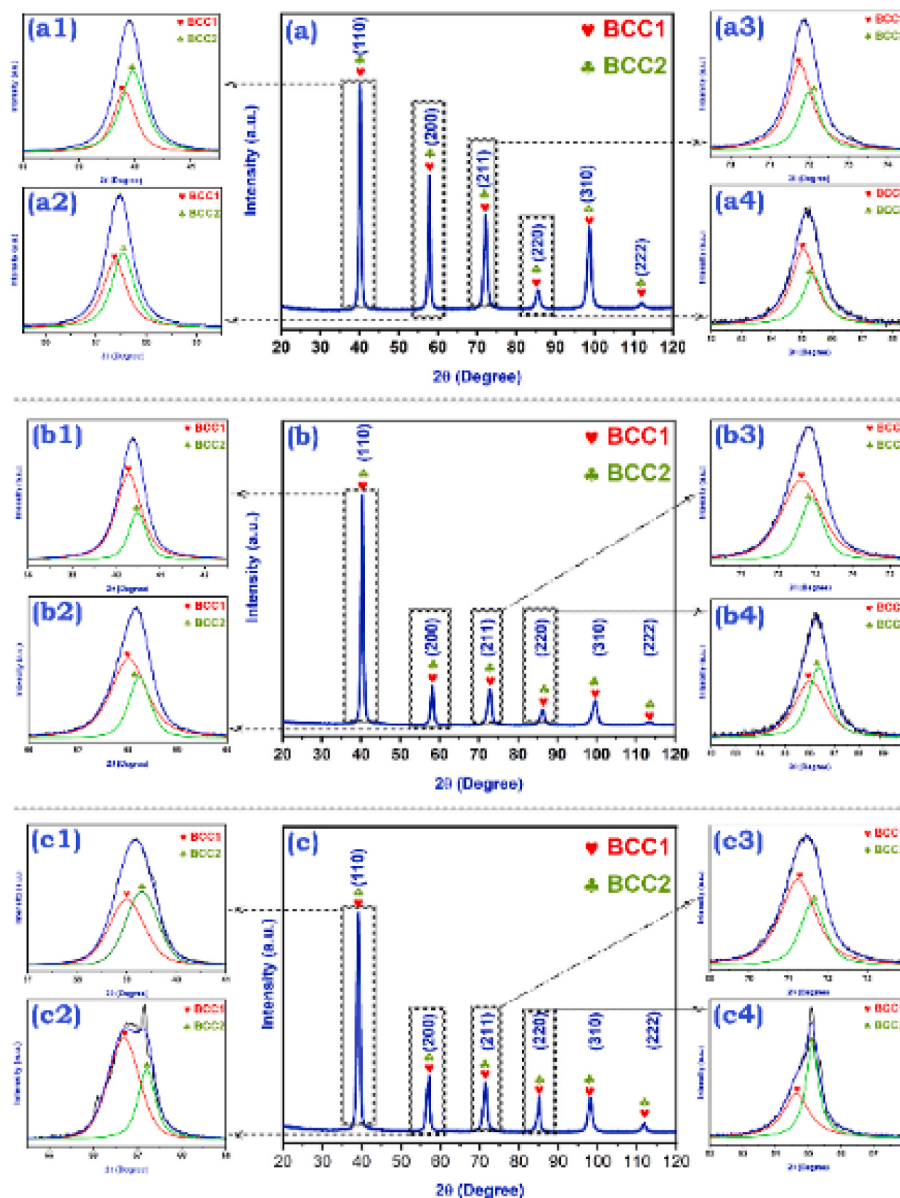


Fig. 1. Phases evolved in the as-cast (a) MoNbTaW (RHEA1); (b) MoNbTiW (RHEA2); (c) MoNbTaTiW (RHEA3). The presence of dual phase BCC structure (BCC1 and BCC2) was discerned through deconvolution of the intense reflections as shown in the a1-a4, b1-b4, c1-c4 for RHEA1, 2 and 3 respectively.

spot patterns corresponding to $\{011\}$ and $\{002\}$ reflection along the $[1\bar{0}0]$ zone-axis of BCC phase. The SAD pattern of RHEA2 shown in Fig. 2 (d) represents spot patterns corresponding to $\{011\}$, $\{200\}$, and $\{211\}$ reflection along the $[01\bar{1}]$ zone-axis of BCC phase. Similarly, the SAD pattern of RHEA3 shown in Fig. 2 (f) represents spot patterns corresponding to $\{011\}$, $\{200\}$, and $\{211\}$ reflection along the $[0\bar{1}1]$ zone-axis of BCC phase. The TEM results were found to be in line with XRD results as depicted in Fig. 1.

Fig. 3 (a), 3 (b) and 3 (c) represents the optical micrograph of RHEA1, 2 and 3 respectively. Fig. 3 distinctly represents dendritic (DR) and inter-dendritic (IDR) regions. The dendritic regions were found to have light contrast and the inter-dendritic regions were found to have dark contrast (Fig. 3). Further, variation in the size of microstructure were observed and can corroborated with the gradient in the cooling rate from bottom to the top of button prepared through vacuum arc melting (VAR) (Fig. 3 (c)). The secondary dendritic arm spacing (SDAS) were found to be $\sim 5.05 \mu\text{m}$, $\sim 4.60 \mu\text{m}$ and $\sim 4.67 \mu\text{m}$ for RHEA 1, 2 and 3 respectively. These SDAS reveals the solidification pattern of RHEAs prepared by VAR. The presence of different elements and their

compositions affect the SDAS. To calculate SDAS fifteen (15) readings were taken at five (5) different locations. The variation in SDAS for MoNbTaW to MoNbTiW (RHEA1 to RHEA3) was found to be linear. The SDAS values were greatly affected by addition of Ti in the RHEA2 and RHEA3, and it decreases with increase in Ti concentration.

The SEM micrograph of MoNbTaW, MoNbTiW, and MoNbTa_{0.5}Ti_{0.5}W RHEAs in back-scattered mode at different magnifications are shown in Fig. 4 (a & b), 4 (c & d), 4 (e & f) respectively. These micrograph represents the formation of dendritic and inter-dendritic morphology in the as-cast RHEAs irrespective of their nominal composition (Table 1). Further, these SEM micrographs shown in Fig. 4 distinctly represents microstructure having BCC phases enriched with different elements as evident form two color contrast i.e. light grey and dark grey. The nominal chemical composition pertaining these phases having slightly different color contrast were ascertained through point-EDS analysis as marked in Fig. 4 (b), 4 (d) and 4 (f) and reported in Table 2. In case of these RHEAs, the light grey contrast was found to be enriched in W, and the dark grey contrast was found to be enriched in Mo and Nb (Table 2). From the SEM micrograph it is evident that the

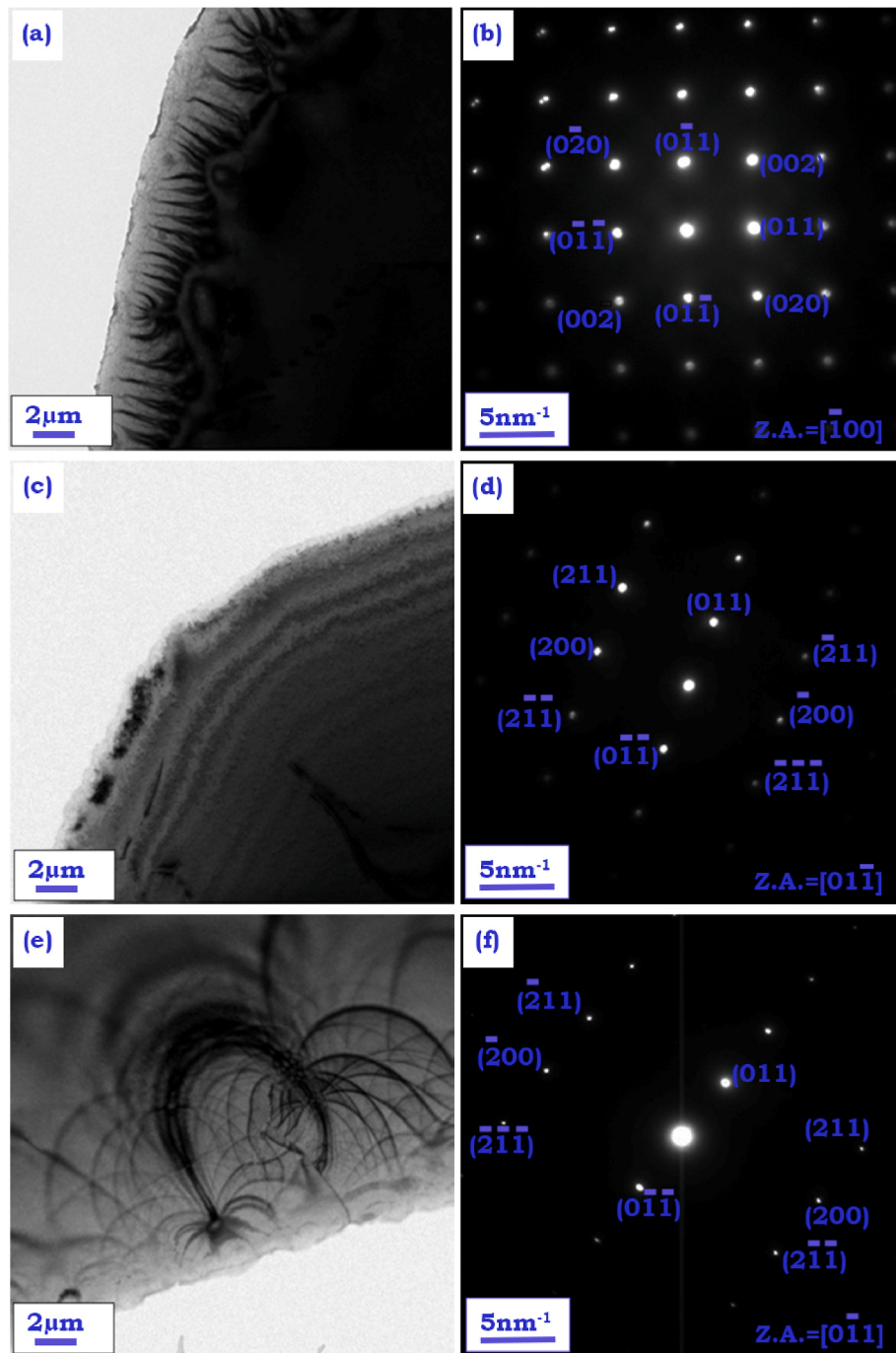


Fig. 2. Diffraction contrast images of the as-cast (a, b) MoNbTaW (RHEA1); (c, d) MoNbTiW (RHEA2); (e, f) MoNbTa_{0.5}Ti_{0.5}W (RHEA3). (a), (c), and (e) represents the bright-field (BF) images of RHEA1, 2 and 3 respectively. (b), (d), (f) represents the selected area diffraction (SAD) pattern of RHEA 1, 2 and 3 corresponding to BF shown in (a), (c), and (e) respectively.

fraction of W enriched DR is $\sim 67\%$, $\sim 72\%$, and 82% for RHEA1, 2 and 3 respectively (Fig. 4). Similarly, the fraction of Mo and Nb enriched IDR is $\sim 33\%$, $\sim 28\%$, and $\sim 18\%$ in RHEA1, 2 and 3 respectively.

The SEM-EDS line scans were used for understanding the elemental distribution in RHEAs as discerned from Fig. 5. Fig. 5 (a), 5 (c), and 5 (e) represents the back-scattered SEM micrograph of RHEA1, 2 and 3 respectively. The corresponding elemental distribution of the alloying elements in the RHEA 1, 2 and 3 were shown in Fig. 5 (b), 5 (d) and 5 (f) respectively. The elemental distribution in the dendritic and inter-dendritic regions were discerned along the arrow (marked in pink color) as evident from Fig. 5 (a), 5 (c), and 5 (e). The dendritic region

were found to be enriched in W, and the inter-dendritic regions were enriched in Mo and Nb for RHEA1 (Fig. 5 (b)). In case of RHEA2, the dendritic regions were seen to be enriched in W, and inter-dendritic were found to be enriched in Mo, Nb and Ti (Fig. 5 (d)). Fig. 5 (f) discerns W enriched dendritic regions, and Mo, Nb and Ti enriched inter-dendritic regions for RHEA3. In all these RHEAs, the elemental distribution of Ta was found to be almost uniform in the dendritic as well as inter-dendritic regions as evident from Fig. 5 (b) and 5 (f). The SEM micrograph discerns elemental micro-segregation in these RHEAs and are consistent with the results observed through XRD (Fig. 1). The BCC1 phase corresponds to the dendritic regions enriched in 'W' (Figs. 1, 4 and

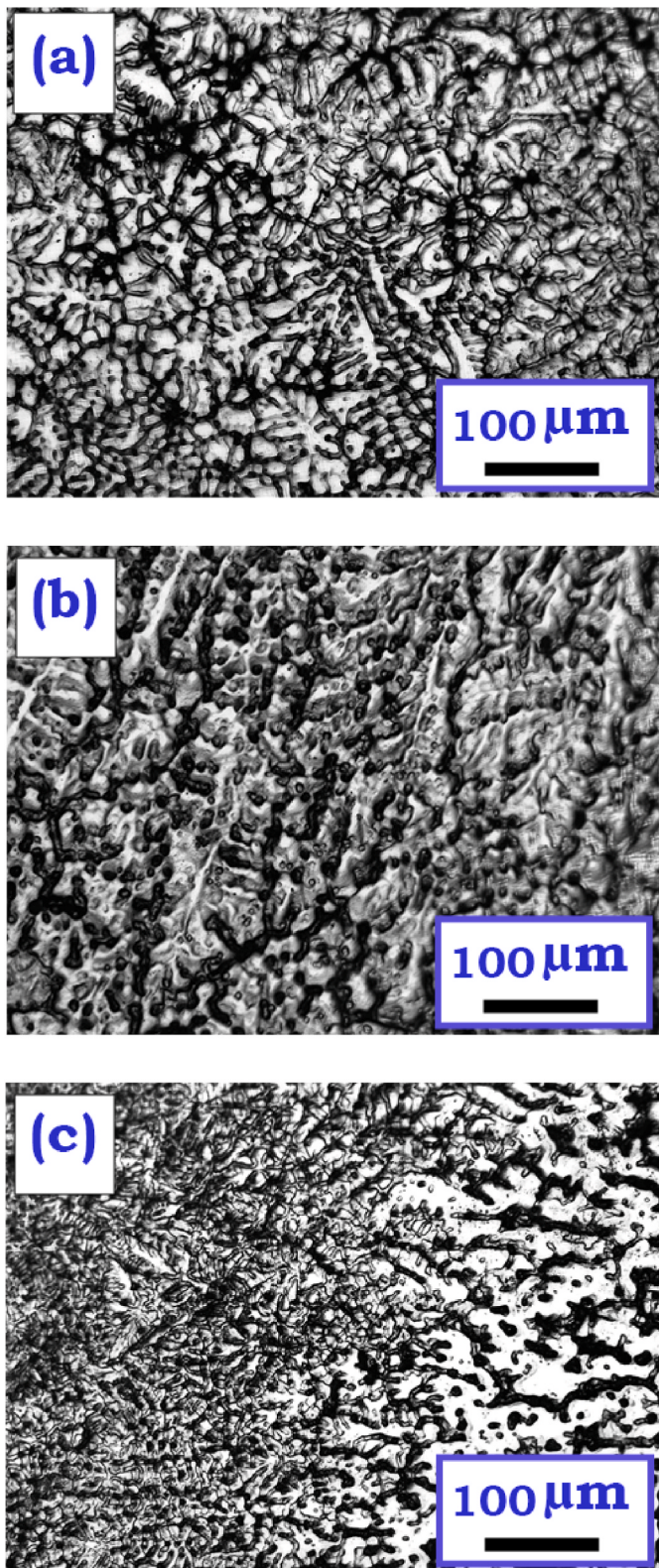


Fig. 3. Optical micrograph of the as-cast (a) MoNbTaW (RHEA1); (b) MoNbTiW (RHEA2); (c) MoNbTa_{0.5}Ti_{0.5}W (RHEA3) showing the presence of dendritic region (DR) and inter-dendritic region (IDR).

5). Similarly, the BCC2 phase corresponds to the inter-dendritic regions enriched in Mo, Nb and Ti ([Figs. 1, 4 and 5](#)).

[Fig. 6](#) discerns the indentation behavior of RHEAs obtained through instrumented microhardness tester. The microhardness and modulus of

elasticity of these RHEAs were computed by Oliver-Pharr method [47] and are reported in [Table 3](#). Efforts were made to compute the microhardness and modulus of elasticity for dendritic and inter-dendritic through instrumented indentation system at low loads. The load-displacement plot for RHEA 1, 2 and 3 were shown in [Fig. 6](#) (a), 6 (b) and 6 (c) respectively. From these plots it is clear that the depth of indentation for RHEA2 is highest (~1.28 μm (DR), ~1.30 μm (IDR)) followed RHEA3 (~0.83 μm (DR), ~0.84 μm (IDR)) and RHEA1 (~0.71 μm (DR), ~0.85 μm (IDR)). From the displacement plot it can be discerned that the RHEA2 has comparatively more plastic deformation compared to RHEA3 and RHEA1 ([Fig. 6](#) (a), 6 (b), & 6 (c)). The addition of Ti in these RHEAs influences the microhardness and also the modulus of elasticity as reported in [Table 1](#). The indents in the DR and IDR regions for RHEA1, 2 and 3 were shown in [Fig. 6](#) (a1 & a2), 6 (b1 & b2) and 6 (c1 & c2) respectively. The addition of Ti in non-equiautomic RHEA (RHEA2) considerable enhances its microhardness (~5.75 GPa) and modulus of eleasticity (~494 GPa) in contrast to that of equiautomic RHEAs ([Table 3](#)).

4. Discussion

The paradigm surge in the alloys design and development strategies has completely redefined the conventional concepts of alloys leading to the formation of solid solution phases [48]. The renaissance in physical metallurgy has enunciated the discovery of high entropy alloys (HEAs) [49]. These multicomponent equiautomic HEAs were found to have single phase solid solution for the first time in the year 2004 by Cantor et al. [2] and Yeh et al. [3] independently. The high entropy effect in these alloys were considered to be responsible for formation of single phase solid solution [48]. However, the recent review article by Steurer [50] has demonstrated that only eighty (80) HEAs composition forms single phase solid solution. Therefore, it is of utmost importance to study the phase evolution in these RHEAs prepared through VAR.

In the present investigation, concentrated efforts were made to understand phase formation in these RHEAs through parametric approach. The various thermodynamic parameters like enthalpy of mixing (ΔH_{mix}), entropy of mixing (ΔS_{mix}), atomic size difference (δ), valence electron concentration (VEC), and electronegativity difference ($\Delta \chi$) were computed for understanding the phase formation in RHEA1, 2 and 3. The enthalpy of mixing (ΔH_{mix}) were calculated through Miedema's model [51] as reported in [Table 4](#). of RHEA1, 2 and 3 was computed to be -7.00, -5.50, and -6.25 kJ/mol and by using first principle calculation [52] as shown in [Table 4](#). The entropy of mixing (ΔS_{mix}) for these RHEA1, 2 and 3 were found to be 11.53, 11.53, and 12.97 J/mol/K computed using Boltzmann's hypothesis [53] ([Table 4](#)). Similarly, the atomic size difference (δ) for RHEA1, 2 and 3 were computed to be 2.31, 2.98 and 2.69 % ([Table 4](#)). These parameters were first proposed by Yang and Zhang [53] for predicting the formation of single phase HEAs. The value of ΔH_{mix} and ΔS_{mix} lying in the range of -22 to 7 kJ/mol and 11–19.5 kJ/mol, and $\delta \leq 8.5$ % predicts the formation of solid solution in these HEAs [54]. The ΔH_{mix} , ΔS_{mix} and δ reported in [Table 4](#) indicates the formation of solid solution in these RHEAs.

Yang and Zhang proposed another parameter known ' Ω ' and VEC for predicting the formation of solid solution [53]. For $\Omega \geq 1$ promotes the formation of solid solution, and on contrary for $\Omega < 1$ promotes the formation of intermetallics. According to Guo et al. [54], the VEC > 8.0 favors the FCC phase, and VEC < 6.87 favors the formation of the BCC phase. For VEC in the range of 6.8–8.0 favors the formation of BCC plus FCC dual phase solid solutions. A few researchers have used electronegativity difference ($\Delta \chi$) for predicting the formation of solid solution in HEAs [54]. Electronegativity indicates the ability of an atom to attract electrons. The electronegativity difference, $\Delta \chi \leq 17.5$ substantially favors the development of solid solution in HEAs. In the present investigation the values of Ω parameter, VEC and $\Delta \chi$ for RHEAs are reported in [Table 4](#). It is evident from [Table 4](#) that both the Ω parameter and VEC favors the formation of BCC solid solution. The various thermodynamic

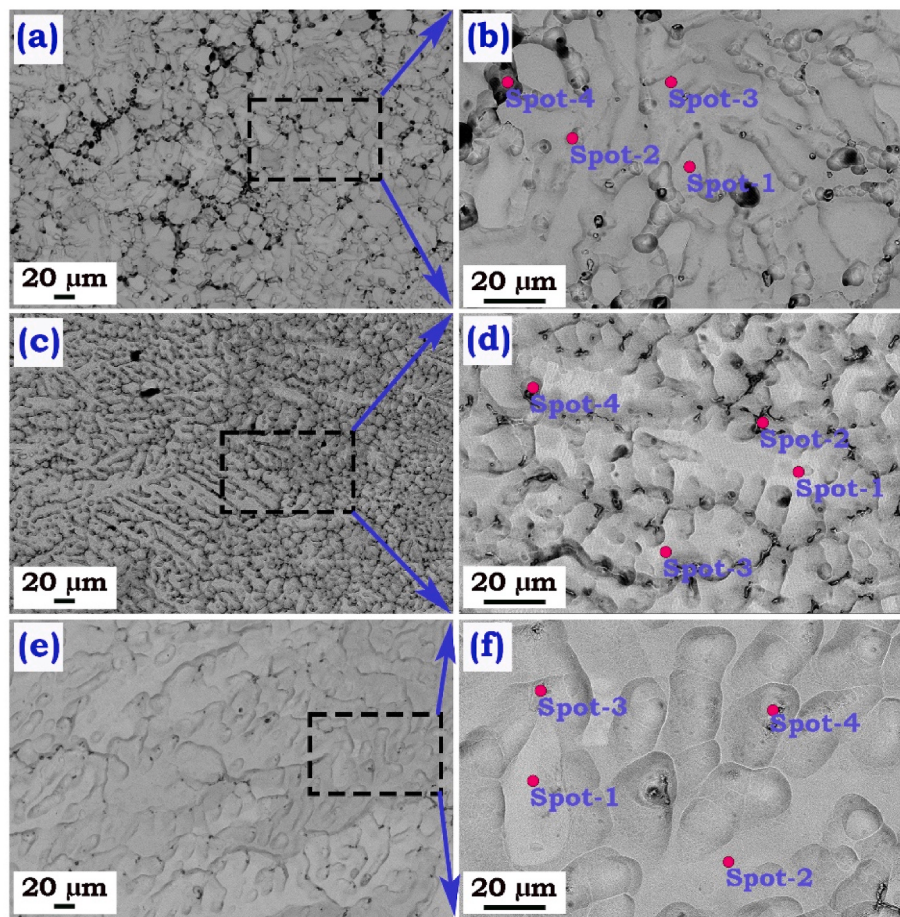


Fig. 4. Back-scattered SEM micrograph of (a, b) MoNbTaW (RHEA1); (c, d) MoNbTiW (RHEA2); (e, f) MoNbTa_{0.5}Ti_{0.5}W (RHEA3) at different magnifications. The EDS point analysis for discerning the nominal chemical composition of DR and IDR in RHEA1, 2 and 3 were marked as Spot 1–4 on SEM micrograph 4 (b), 4 (d) and 4 (e) respectively. The nominal chemical composition of Spot 1–4 for RHEA1, 2 and 3 were mentioned in Table 2.

Table 2

The nominal composition of DR and IDR in RHEAs through EDS point analysis.

Sample Designation	Area	Elements (at %)				
		Mo	Nb	Ta	Ti	W
MoNbTaW (RHEA1)	Full Spectrum	28.44	22.60	27.56	–	21.40
	Spot-1	24.58	16.92	28.89	–	30.01
	Spot-2	31.00	24.99	22.3	–	24.02
	Spot-3	23.92	23.42	26.97	–	26.55
	Spot-4	28.87	27.38	25.58	–	21.11
MoNbTiW (RHEA2)	Full Spectrum	28.90	29.21	–	16.01	25.88
	Spot-1	30.4	32.11	–	9.36	29.3
	Spot-2	26.63	35.14	–	24.03	14.2
	Spot-3	32.13	22.57	–	19.62	34.32
	Spot-4	32.51	34.42	–	25.39	7.67
MoNbTaTiW (RHEA3)	Full Spectrum	27.95	28.71	12.53	9.9	21.91
	Spot-1	25.79	31	14.62	4.84	23.75
	Spot-2	26.81	25.02	12.99	7.98	27.2
	Spot-3	28.15	28.09	12.2	12.33	19.23
	Spot-4	27.69	37.57	9.02	10.8	14.92

parameters suggested the formation of BCC phase solid solution. However, the present investigation suggests the formation of dual phase BCC solid solution as evident from Fig. 1.

A few recent investigations have suggested influence of other parameters like melting point, self-diffusion co-efficient etc. responsible for phase formation during synthesis of HEAs through powder

metallurgical processing [37,55,56] and VAR [6]. The physical and mechanical parameters of individual alloying elements are mentioned in Table 5. Mukhopadhyay and co-workers have made systematic efforts in understanding the phase evolution/formation in a few HEAs as a function of melting point and self-diffusion co-efficient of individual alloying elements [37,55–59]. In general the elements with high melting point have higher bond strength. In an investigation, Chen et al. [60] have observed that the element with high melting points have low alloying rate. Further, Shivam et al. [57] and Singh et al. [37] have introduced the concept of host lattice in these HEAs. They have observed that the higher melting point elements act as a host lattice [37,57]. Most of the literature available on MoNbTaW RHEAs with or without addition of Ti have reported the formation of single phase BCC solid solution [26]. However, the de-convolution of XRD pattern in Fig. 1 confirmed the presence of BCC solid solution phases having lattice parameter very close to each other due to the effect of micro-segregation in these RHEAs. In the present investigation, it was discerned from Fig. 1 and Table 1 that the BCC1 and BCC2 phase in RHEAs were having lattice parameters close to W (cl2, $a = 3.165 \text{ \AA}$) and Mo (cl2, $a = 3.147 \text{ \AA}$). Therefore, the BCC1 and BCC2 phases in these RHEAs were having W-type and Mo-type host lattice. The SQS of these RHEAs were generated using DFT and the atomic arrangements of the atoms in the supercell consisting of ‘160’ atoms are shown in Fig. 8. The lattice parameter of RHEAs were computed through DFT and mentioned in Table 1. The lattice parameter of RHEAs were in close approximation with experimental findings.

The homogenous elemental distribution is seldom observed in as-cast MoNbTaW RHEAs with or without Ti [15,26]. For overcoming the issue

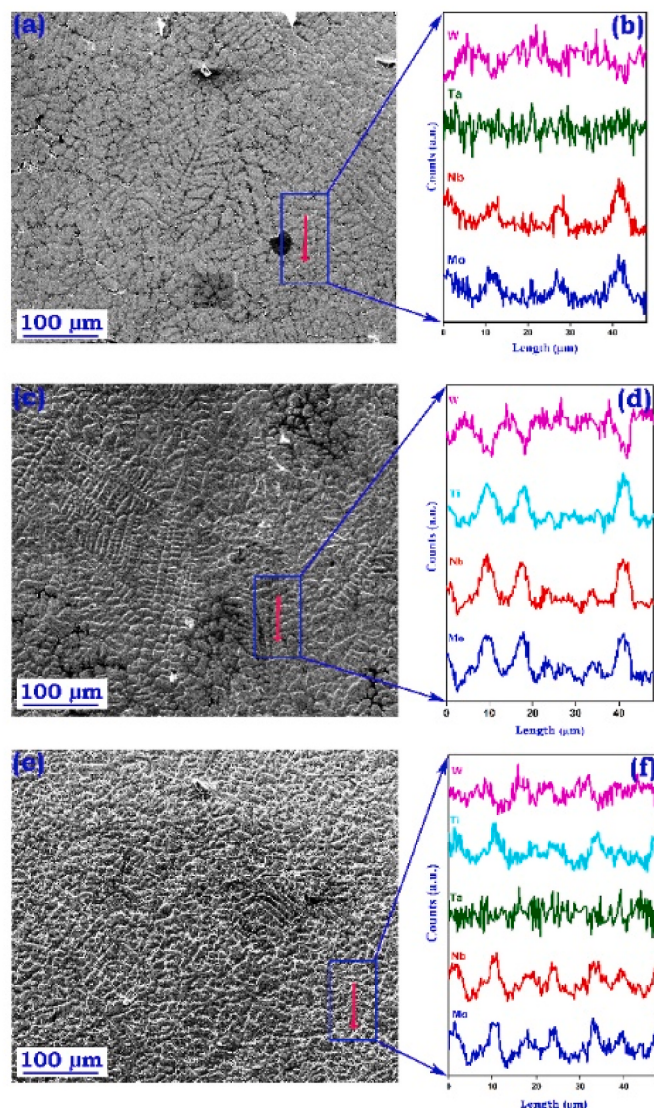


Fig. 5. The SEM-EDS line scans used for understanding the elemental distribution in RHEAs. Back-scattered SEM micrograph of (a) MoNbTaW (RHEA1); (c) MoNbTiW (RHEA2); (e) MoNbTa_{0.5}Ti_{0.5}W (RHEA3) respectively showing the presence of DR and IDR. The corresponding elemental distribution of the alloying elements in the (b) RHEA 1; (d) RHEA2; (f) RHEA3 along the interfaces of DR and IDR.

pertaining the elemental segregation, these RHEAs were re-melted at least 5–6 times. In the present investigation, the RHEAs were found to have DR and IDR regions as shown in Fig. 3. The nominal composition of the DR and IDR were ascertained through SEM-EDS (Figs. 4 and 5, Table 2). These suggested the segregation of elements in DR and IDR regions (Fig. 5 and Table 2). The non-uniformity in chemical composition is generally termed as micro-segregation. The different solidification temperature associated with each element in these RHEAs may be responsible for elemental segregation. The segregation of heavier elements like W and Ta was more prominent in DRs, and partial segregation of Mo and Nb were found in IDR in the RHEAs. In MoNbTiW RHEA, the segregation of heavier elements like W is predominantly in DR, and comparatively lighter elements like Mo, Nb and Ti were segregated in RHEAs. The melting point of elements plays a significant role in micro-segregation behavior in RHEAs during solidification [8]. During solidification elements having higher melting points like W and Ta segregates in DR, and vice-versa was observed for elements having comparatively lower melting points like Mo, Nb and Ti. The solute

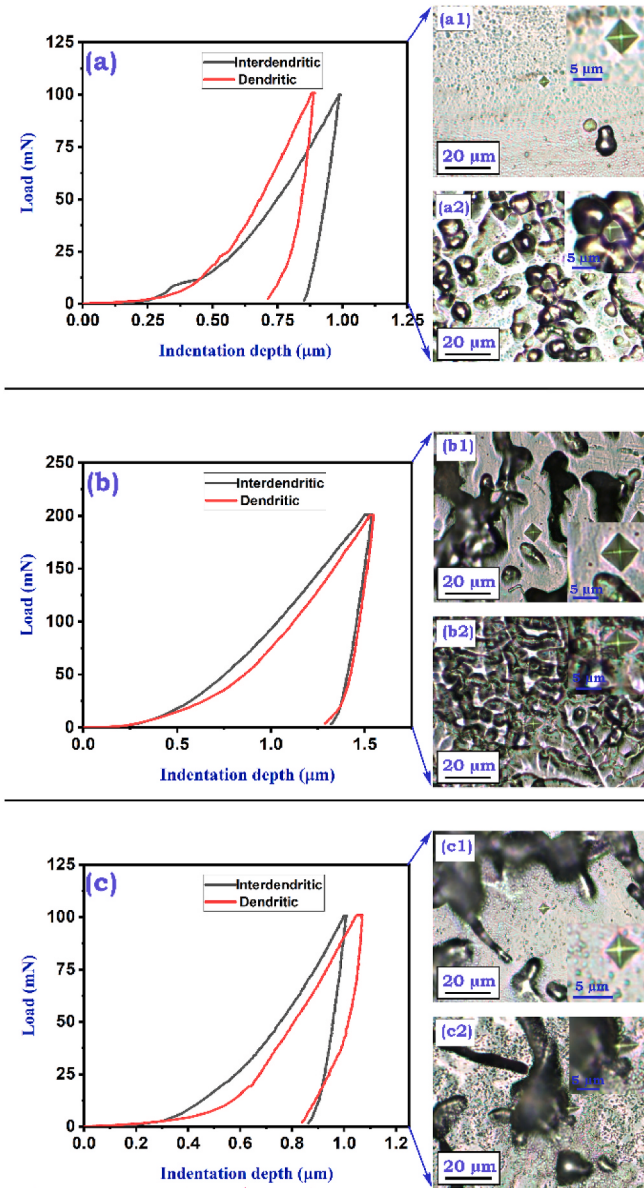


Fig. 6. The load-displacement plot for (a) RHEA 1; (b) RHEA2; (c) RHEA3 at low loads for DR and IDR is shown with red and black colours respectively. The optical micrograph of the indents in the DR and IDR regions for (a1 & a2) RHEA1; (b1 & b2) RHEA2; (c1 & c2) RHEA3 respectively.

rejected and encircled by the secondary arm during solidification gives rise to micro-segregation. A few previous investigations have also suggested the formation of dendritic and inter-dendritic regions in these kind of RHEAs composition [6,10,15,25,26,28,61]. In 2015 Zhang et al. [25] reported the formation of DR (enriched with Ta and W) and IDR (enriched with Ti, V and Nb) in MoNbTaTiVW RHEA. In recent times Kanchi et al. [24] studied the formation of DR and IDR in MoNbTaW RHEA homogenized at 1400 °C (1673 K) for 20 h. They have reported that the DR were found enriched in W, and IDR were enriched in Mo and Nb [24].

The extent of element segregation depends on different solidification temperatures accompanying each element in the alloy system [62]. The micro-segregation in these RHEAs can be quantified with the help of two approaches namely (i) linear [63] (ii) exponential [62]. The Equation-1 mentioned below can be used to describe the micro-segregation using linear approach:

Table 3

Mechanical properties of RHEAs through instrumented indentation and strengthening mechanism.

Sample designation		Elastic Constant (GPa)	MoNbTaW		MoNbTiW		MoNbTa _{0.5} Ti _{0.5} W	
			RHEA1		RHEA2		RHEA3	
			DR	IDR	DR	IDR	DR	IDR
Elastic Constant (GPa)	Experimental	229	232	232	242	253	296	
Hardness (GPa)	SQS	222		243		227		
	Experimental	4.48	4.81	4.81	5.33	4.69	5.75	
	SQS	4.46		4.79		3.58		
	Strengthening mechanism	Solid solution strengthening	4.86		5.16		5.01	
		Dislocation strengthening	0.27		0.30		0.36	
		Grain size strengthening	0.15		0.15		0.18	
		Total contribution	5.28		5.61		5.55	

Table 4

Thermodynamic parameters of RHEAs.

Parameters	Composition			
	MoNbTaW	MoNbTiW	MoNbTa _{0.5} Ti _{0.5} W	
Enthalpy of mixing (kJ/mol)	SQS	-7.07	-6.55	-6.57
	Miedema	-7.00	-5.50	-6.25
Ideal configurational entropy ΔS_{mix}	$S_{mix} = -R \sum_{i=1}^n c_i \ln c_i$ (J/mol/K)	11.53	11.53	12.97
Melting temperature (K) $T_m = \sum_{i=1}^n c_i (T_m)_i$		3157	2819	2988
Omega factor (Ω) $\Omega = \frac{T_m \Delta S_{mix}}{ \Delta H_{mix} }$		5.15	4.96	5.89
Valence electron concentration (VEC)		5.50	5.25	5.37
Electronegativity ($\Delta\chi$) $\Delta\chi = \sqrt{\sum_{i=1}^n c_i (\chi_j - \bar{\chi})^2}$		0.399	0.353	0.358
Atomic size difference (δ) $\delta_r = \sqrt{\sum_{i=1}^n c_i (1 - r_i)^2}$		2.31	2.98	2.68

Table 5

Physical and mechanical properties of alloying elements in RHEAs.

Element	Mo	Nb	Ta	Ti	W
Crystal structure	A2	A2	A2	A3 at R.	A2
Atomic radius, r (nm)	0.136	0.142	0.147	0.146	0.136
Lattice Parameter, a (nm)	0.314	0.330	0.330	0.327	0.316
Young's modulus, E (GPa)	329	105	186	116	411
Poisson's ratio, ν	0.29	0.39	0.34	0.36	0.28
Melting temperature, T_m (K)	2893	2750	3290	1941	3695
Valence electron concentration, VEC	6.0	5.0	5.0	4.0	6.0
Vickers microhardness, H_v (GPa)	1.53	1.32	0.87	0.97	3.43
Yield strength σ_y (MPa)	420	240	170	195	550
Elastic constant (E/GPa)	329	105	186	116	411

$$\Delta c = k [(T_m)_i - T_m] \quad (1)$$

where k is a constant, $(T_m)_i$ is the melting point of the i th element, and $T_m = \sum c_i (T_m)_i$ is the average melting temperature of RHEAs using rule of mixture (Table 5). The value of ' Δc ' reflects the amount of element segregation between the dendritic and inter-dendritic region. The amount of elemental segregation (Δc) is shown in Table 6. In the alloy MoNbTaW elements Mo and Nb has elemental segregation, $\Delta c < 1$; whereas Ta and W has $\Delta c > 1$. In the RHEA3, elements Mo and W has $\Delta c > 1$; whereas elements Nb and W has $\Delta c < 1$. Similarly, in RHEA2 elements such as Mo, Nb and Ti has $\Delta c < 1$; whereas elements like Ta and W > 1 . The elements having $\Delta c > 1$ will segregate into dendritic regions, and elements having $\Delta c < 1$ will segregate in inter-dendritic regions. The elements like W and Ta having higher melting points segregate into dendritic region, whereas Mo, Nb and Ti having lower melting temperature segregate into inter-dendritic region also evident in the present

Table 6

Prediction of the elemental segregation (Δc) in RHEAs using linear approach.

Composition		MoNbTaW (RHEA1)	MoNbTiW (RHEA2)	MoNbTaTiW (RHEA3)
Alloy melting temperature (K)		3157	2819	2988
Elements	Mo	Elemental segregation	-264	-95
	Nb		-407	-238
	Ta	(Δc)	133	301
	Ti		-	-878
	W		538	-1047
			875	706

investigation (Figs. 4 and 5, Table 6). The Equation-2 mentioned below can be used to describe the micro-segregation using exponential approach:

$$K = e^{0.0013\Delta T} \quad (2)$$

where $\Delta T_i = T_m^i - T_m^{mix}$; T_m^i is the melting temperature of i th element, and T_m^{mix} is the melting temperature of alloy using rule of mixture. It is clear from Equation-2 that the elements having $\Delta T > 0$ will have $K > 1$, and $\Delta T < 0$ have $K < 1$. The elements with $K > 1$ will solidify first in the melt and vice-versa for other elements. This behavior is obeyed by all elements in the alloys [64]. During solidification dendrite grows into the melt, and the secondary arm spreads from the primary (main) dendrite. The solute is rejected and encircled by the secondary arm during this process, which gives rise to micro-segregation during solidification. The extent of element segregation depends on different solidification temperatures accompanying each element in the alloy system [64]. For quantifying micro-segregation, the partition coefficient $K = C_{dr}/C_{idr}$ has been generally used and computed for alloying elements in these RHEAs as shown in Fig. 8 and reported in Table 7. The ' K ' associated with the element's melting temperature (T_m), and K also correlate the distribution of each element in excess/deficient in the dendritic arm (where dr = dendritic; idr = inter-dendritic). This phenomenon can be explained from Fig. 7. The partition coefficient (K) of Ta and W was found to be greater than one (Fig. 7 and Table 7). Therefore, W and Ta in the RHEA1 and 2 is expected to solidify first from the melt resulting in the formation of DR (Figs. 4 and 5). The elements having $K < 1$ will solidify later, and lead to the formation of IDR (Figs. 4 and 5). In an investigation Yao et al. [65] discerned the formation of DR and IDR based on the values of K . It is evident from Fig. 7 that the partition co-efficient (K) for W and Ta is well

Table 7

Prediction of the partition coefficient (K) in RHEAs using an exponential approach.

Elements	MoNbTaW	MoNbTiW	MoNbTa _{0.5} Ti _{0.5} W
Mo	0.712	1.106	0.977
Nb	0.583	0.905	0.800
Ta	1.194	-	1.638
Ti	-	0.319	0.282
W	2.013	3.125	2.762

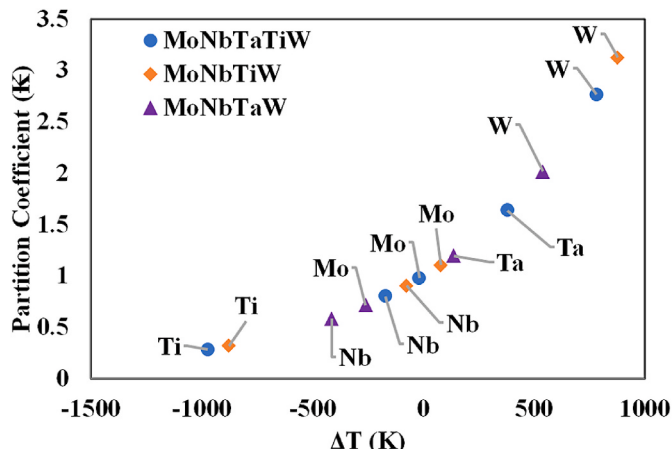


Fig. 7. The correlation between the partition coefficient, $K = C_{\text{dr}}/C_{\text{idr}}$, and the difference, $\Delta T = (T_m)_i - T_m^{\text{mix}}$.

above the threshold desired for the formation of DR in these RHEAs. Similarly, the partition co-efficient (K) for Ti, Nb and Mo was found to be less than or almost equal to the threshold desired for the formation of IDR.

The RHEAs were found to have excellent microhardness without any signature of crack formation (Fig. 6 and Table 8). Efforts were made to investigate the microhardness and modulus of elasticity of the DR and IDR independently using instrumented indentation system at low loads (Fig. 6). In all the RHEA composition the microhardness and modulus of elasticity (E) of IDR were comparatively more than the DR (Table 8). For the first time systematically efforts were made to compute the microhardness of the DR and IDR in these RHEAs. In all the previous investigation, researchers and co-workers have reported the microhardness comprising of contribution from DR and IDR in MoNbTaW based RHEAs [11,15,24–26,28]. The first report on the RHEA by Senkov et al. [10,28] reported the microhardness of MoNbTaW and MoNbTaWV RHEAs to be

~4.45 GPa and ~5.25 GPa respectively. Zhang et al. [25] reported the microhardness of ~5.0 GPa for MoNbTaTiV RHEA comprising of DR and IDR. Similarly, Kanchi et al. [24] have reported the microhardness for as-cast and homogenized MoNbTaW RHEA to be ~4.69 GPa and ~5.68 GPa respectively. The microhardness in the present investigation were in accordance with the previous findings, however the microhardness in these RHEAs were found to be greatly influenced by the local compositional fluctuations in the DR and IDRs (Table 2).

The mechanical properties of these RHEAs were modelled with the help of strengthening mechanism and density functional theory. The elastic constants are essential mechanical property of materials. The most obvious and direct application of elastic constants is to evaluate the elastic strain or energy change of materials under various stresses from external, internal, and thermal sources. Elastic constants can also provide information about stability, stiffness, brittleness, ductility, and anisotropy of materials. Elastic constant derivation and conversion relates mechanical properties. Three elastic constant C_{11} , C_{12} and C_{44} are sufficient for defining the cubic system. For mechanically stable structure $C_{11} > 0$, $C_{44} > 0$, $C_{11}-C_{12} > 0$ and $C_{11} + 2C_{12} > 0$ must satisfy.

The theoretical elastic constants C_{ij} , $(C_{11}-C_{12})$, $(C_{11} + 2C_{12})$, the tetragonal shear modulus, $\bar{C} = (C_{11}-C_{12})/2$ and the Cauchy pressure, $C_p = C_{12}-C_{44}$ for the RHEA1, 2 and 3 were calculated by DFT. They all satisfy the given mechanical stability conditions. The physical and mechanical properties of RHEA such as bulk modulus (B), shear modulus (G), Young's modulus (E) and Poisson's ratio (ν) were computed using the values of elastic constants with the help of Voigt-Reuss-Hill (VRH) average scheme [66–68]. The VRH approximation gives the valid values of the bulk and shear modulus. For the cubic system, the Voigt bounds of the bulk modulus B_v and the shear modulus G_v are mentioned below:

$$B_v = \frac{C_{11} + 2C_{12}}{3} \quad (3)$$

$$G_v = \frac{(C_{11} - C_{12} + 3C_{44})}{5} \quad (4)$$

The Reuss bounds of the bulk modulus B_R and shear modulus G_R are:

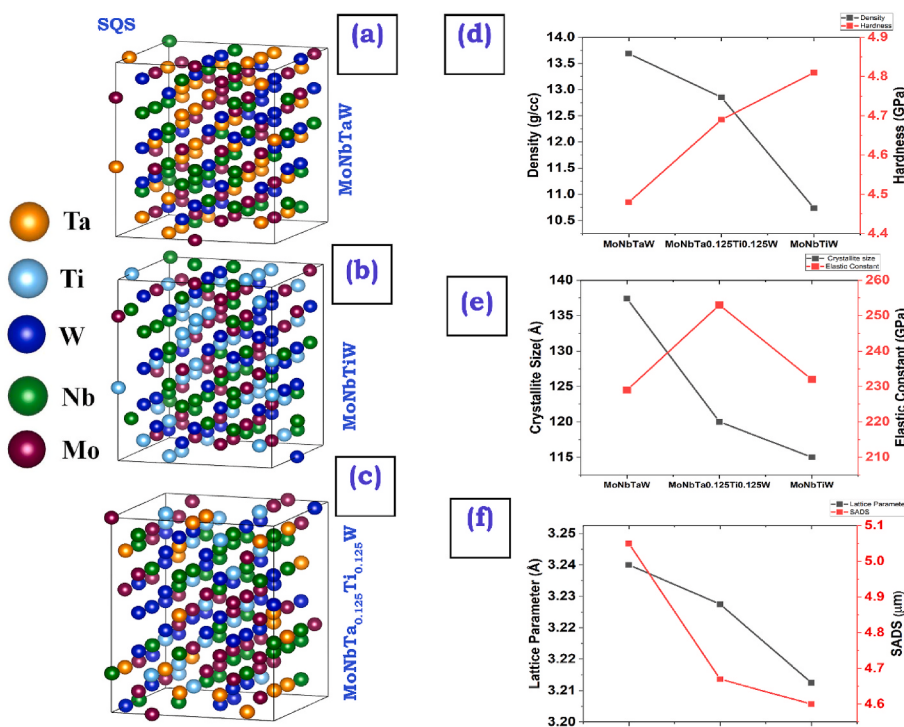


Fig. 8. Schematic representation of Special quasi-random structures (SQS) of (a) MoNbTaW; (b) MoNbTiW; (c) MoNbTaTiW. Comparison of various parameters (d) Density and Hardness – three different alloys (e) Crystallite size and Elastic Constant – three different alloys (c) Lattice Parameter and SADS – three different alloys.

$$B_R = B_V \quad (5)$$

$$G_R = \frac{5C_{44}(C_{11} - C_{12})}{4C_{44} + 3(C_{11} - C_{12})} \quad (6)$$

Finally, Hill has proved that Voigt and Reuss's boundaries are strict upper and lower bounds. Then, the bulk modulus ' B ' and shear modulus ' G ' based on Hill [66] approximation can be estimated from these boundaries such as

$$B = \frac{B_V + B_G}{2} \quad (7)$$

$$G = \frac{G_V + G_R}{2} \quad (8)$$

Therefore, Young's modulus (E) and Poisson's ratio (ν) can be converted based on Hill's elastic modulus (B) and (G), which can be expressed as:

$$E = \frac{9BG}{3B + G} \quad (10)$$

$$\nu = \frac{3B - 2G}{2(3B + G)} \quad (11)$$

The DFT driven calculation of the modulus and the Poisson's ratio are listed in Table 8. The elastic constant obtained using SQS is in good agreement in MoNbTaW and MoNbTiW system. Whereas in quinary RHEA, the experimental findings were having slight deviation with the DFT calculations. The possible reason for such an anomaly may be the number of atoms considered in generating the SQS in these non-equiautomatic RHEAs.

The microhardness predicted through DFT calculations were also found to be in good agreement with experimental results for MoNbTaW and MoNbTiW system using SQS model (Fig. 8). However, deviation in the microhardness from DFT and experimentation was observed in case of quinary non-equiautomatic RHEA (Table 3 and Fig. 8). The modulus of elasticity for RHEA1 and RHEA3 obtained using rule of mixture (ROM) were found to be in close approximation with those predicted through DFT and experimentation (Table 3 and Fig. 8).

The bulk modulus B is typically used to characterize the measure of resistance to volume changes by the applied pressure. The stiffness of materials is usually characterized by modulus E and G . The Poisson's ratio ν ranges from $0 < \nu < 0.5$. When Poisson's ratio is 0.5, it means that volume remains constant under tensile or compressive tests. If Poisson's ratio slightly less than 0.5 means that the material slightly increases in volume when subjected to tensile stress and slightly decreases in volume when subjected to compressive stress. The larger the Poisson's ratio ν value, the better the plasticity of the material. Moreover, $B/G > 1.75$, and $\nu > 0.30$ both meet the Pugh standard for the definition of ductile materials. While using SQS model all three RHEAs showed ductile behavior theoretically. The ductility in quaternary RHEA2 was found to be highest, however nominal increase in the ductility from MoNbTaW to MoNbTiW was reported (Table 8). The theoretical findings were in line with the experimental results for microhardness. The load-displacement curve for RHEA2 has shown the highest plastic deformation compared the RHEA1 and 2 (Fig. 6 (a), 6 (b) and 6 (c)). Similarly, the optical

micrograph showing the indentation in the DR and IDR does not show any signature of indentation cracks, enunciating the fact that these RHEAs are ductile in nature as observed theoretically. Another parameter known as Cauchy relation (C_P) used to represent the brittleness or ductility of materials [69]. The Cauchy relation defined as $C_P = C_{12} - C_{44}$. If the value of the C_P is positive, the material should be plastic, and vice-versa for brittle materials. As per the Cauchy criteria, all the RHEAs in the present investigation behaves plastically. These finding were also in accordance with the present findings as observed in Fig. 6.

Further, the mechanical properties of these RHEAs were also understood with the help of strengthening mechanisms operative in this kind of alloy systems. The yield strength (YS) and microhardness (H_v) data using rule of mixture (ROM) for individual elements and the RHEAs is shown in Table 5. The Tabor's equation [70] used here to calculate the YS of alloys as shown in equation (12):

$$\sigma_{0.2} = \frac{H_v}{3} \quad (12)$$

From Tables 3 and 5 and it is clear that the microhardness and yield strength values do not obey the values computed from ROM. Similar findings have been reported in RHEA in previous studies [71]. Therefore, various other factors contributing to the overall strength of alloys needs to be taken in to consideration. The other factors contributing to the overall strength are (i) solid solution strengthening (σ_{sss}), (ii) grain size strengthening (σ_{gss}), (iii) precipitation strengthening (σ_{ps}), and (iv) dislocation strengthening (σ_{ds}). Among these parameters, the solid solution strengthening is most likely responsible for the alloy's extraordinary microhardness and YS. In the present investigation, contribution from precipitation can be neglected. The contribution from the various factors on the microhardness of these RHEAs have been shown in Fig. 9 and Table 3. The high-hardness in these RHEAs were due to solid solution strengthening as observed from Table 3. The detailed explanation of all these factors are mention in supplementary section.

Fig. 8 shows the structures used in the calculation of elastic constant, hardness, Poisson's ratio and B/G ratio. The adjoining names corresponds to the alloy used in this calculation where different color balls correspond to different elements. Fig. 8 (d) the composition – hardness

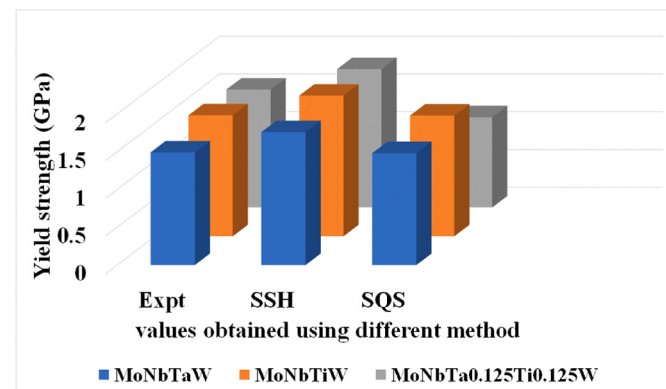


Fig. 9. Comparing the yield strength of three different alloys using different model with experimental values.

Table 8
A comparative study of Elastic constant values obtained computational methods (SQS).

Method	Composition	Elastic constant (in GPa)								
		C11	C12	C44	C11-C12	C11+2C12	C' (C11-C12)/2	Cp C12-C44	B/G	ν
SQS	MoNbTaW	391	174	59	216	741	108	114	3.06	0.35
	MoNbTiW	426	191	66	234	809	117	125	3.00	0.35
	MoNbTa _{0.5} Ti _{0.5} W	354	166	56	188	686	94	109	3.18	0.36

diagram can be discussed on the basis of VEC. There is inverse relation exist between VEC and hardness of alloys. The VEC of alloy MoNbTaW is 5.5 and hardness of major phase is 4.46 GPa whereas VEC of alloy MoNbTiW is 5.25 and having hardness of major phase 4.81 GPa in the similar way VEC of alloy MoNb(TaTi)W is 5.37 and hardness is 4.69 GPa. Similar relation has been observed by Balasubramanian et al. [72] for his study on carbides, nitrides and carbonitrides. Fig. 7 (e) showing variation of elastic constant and crystallite size with composition. All these alloys are ductile in nature ($B/G > 1.75$ and $\nu > 0.3$). The B/G ratio and ν value of MoNbTa_{0.5}Ti_{0.5}W is higher than rest of two alloys, suggesting higher ductility. The result of higher ductility of MoNbTa_{0.5}Ti_{0.5}W is supported by higher elastic constant. This phenomenon can be explained on the basis of dislocation strengthening. The dislocation available in quinary non-equiautomatic alloy is more in comparison to quaternary alloys. Fig. 8 (f) show a good trend of variation of lattice parameter and SADS in the alloy. The reason for decrease in SADS has been already explained above. The appreciable value of hardness along with detailed understanding of the structure and microstructure of these dual-phase RHEAs envisages its potential usage for high-temperature structural materials.

5. Conclusion

The following conclusions can be drawn from present investigation on MoNbTaW, MoNbTiW and MoNbTa_{0.5}Ti_{0.5}W RHEAs.

1. A BCC solid solution phases (BCC1 & BCC2) having very close lattice parameter were found to exist in MoNbTaW MoNbTiW and MoNbTa_{0.5}Ti_{0.5}W RHEAs. The BCC1 and BCC2 in RHEAs were found to have W-type and Mo-type BCC host lattice.
2. Microstructure of these RHEAs were found to comprise of dendritic and inter-dendritic regions enriched in W and Ta, and Mo, Nb and Ti respectively. Further, the addition of Ti influenced the SADS in these RHEAs and was found to decrease with increase in Ti content.
3. The enthalpy of mixing, entropy of mixing, atomic size difference, VEC, and electronegativity suggested the formation of single BCC solid solution. However, the micro-segregation in these RHEAs predicted through linear and exponential approach for RHEAs envisages the formation of microstructure having DR and IDR enriched in W and Ta, and Mo, Nb and Ti respectively. The elemental segregation in the DR and IDR might be responsible for the appearance of BCC1 and BCC2.
4. The microhardness and modulus of elasticity (E) of BCC RHEAs were found to be varying for DR and IDR regions enriched in W and Ta, and Mo, Nb and Ti. The microhardness for DR and IDR can be tuned in the range of ~4.48–4.81 GPa and ~4.81–5.75 GPa respectively. Similarly, the modulus of elasticity for DR and IDR was found in the range of ~229–253 GPa and ~232–494 GPa respectively. The microhardness and E were found to be dependent on the fraction of Ti in MoNbTaW RHEAs.
5. The structure and mechanical properties of RHEAs were understood with the help of DFT. The value of lattice parameter, microhardness and modulus of elasticity were in good agreement with experimental results. The B/G ratio computed through DFT confirmed the ductility in these RHEAs as also evident from the absence of indentation cracks even at higher loads.
6. The high microhardness in these RHEAs were explained on the basis of different strengthening mechanism. The contribution of solid solution hardening was mainly contributing to the high hardness in these RHEAs.

Credit authorship contribution statement

Shanker Kumar: Conceptualization, Investigation, Formal analysis, Methodology, Writing-Original draft; **Albert Linda:** Data Curation, Methodology, Investigation; **Yagnesh Shadangi:** Investigation, Formal

analysis, Methodology, Writing – Review and Editing; **Vikas Jindal:** Supervision, Resources, Conceptualization, Formal analysis, Writing-Review and Editing.

Declaration of competing interest

The authors declare that they have no known competing financial interests or personal relationships that could have appeared to influence the work reported in this paper.

Data availability

Data will be made available on request.

Acknowledgement

Authors thankfully acknowledges help of Profs. S Lele and N. K. Mukhopadhyay for needful discussion. Authors acknowledge the support of Profs. R. K. Mandal, N. K. Mukhopadhyay, and Drs. K. Chattopadhyay and R. Manna for XRD, instrumented indentation testing, wire-EDM and ICDD database respectively. Authors also acknowledge the Central Instrument Facility (CIF), IIT BHU Varanasi for the scanning electron microscope facility. VJ expresses gratitude towards the DST, Government of India for the SERB sponsored project (Project No. EMR/2017/004309). SK thanks Priyatosh Pradhan for help in instrumented indentation testing.

Appendix A. Supplementary data

Supplementary data to this article can be found online at <https://doi.org/10.1016/j.intermet.2023.108080>.

References

- [1] B. Murty, J. Yeh, S. Ranganathan, P. Bhattacharjee, *High-Entropy Alloys*, second ed., Elsevier, 2019.
- [2] B. Cantor, I.T.H. Chang, P. Knight, A.J.B. Vincent, Microstructural development in equiautomatic multicomponent alloys, *Mater. Sci. Eng.* 375 (377) (2004) 213–218, <https://doi.org/10.1016/j.mse.2003.10.257>.
- [3] J.W. Yeh, et al., Nanostructured high-entropy alloys with multiple principal elements: novel alloy design concepts and outcomes, *Adv. Eng. Mater.* 6 (5) (2004) 299–303, <https://doi.org/10.1002/adem.200300567>.
- [4] S. Gorse, D.B. Miracle, O.N. Senkov, Mapping the world of complex concentrated alloys, *Acta Mater.* 135 (2017) 177–187, <https://doi.org/10.1016/j.actamat.2017.06.027>.
- [5] T.P. Yadav, S. Mukhopadhyay, S.S. Mishra, N.K. Mukhopadhyay, O.N. Srivastava, Synthesis of a single phase of high-entropy Laves intermetallics in the Ti-Zr-V-Cr-Ni equiautomatic alloy, *Philos. Mag. Lett.* 97 (12) (Dec. 2017) 494–503, <https://doi.org/10.1080/09500839.2017.1418539>.
- [6] V.K. Pandey, Y. Shadangi, V. Shivam, B.N. Sarma, N.K. Mukhopadhyay, Theoretical and experimental study on phase stability of TiVZrMoW refractory high entropy alloy, *Philos. Mag. A* 102 (6) (2022) 480–503, <https://doi.org/10.1080/14786435.2021.2001066>.
- [7] O. Senkov, G. Wilks, D. Miracle, C. C.- Intermetallics, and U. 2010, “Refractory high-entropy alloys,” *Intermetallics* 18 (2010) 1758–1765.
- [8] O.N. Senkov, D.B. Miracle, K.J. Chaput, J.P. Couzinie, Development and exploration of refractory high entropy alloys - a review, *J. Mater. Res.* 33 (19) (2018) 3092–3128, <https://doi.org/10.1557/jmr.2018.153>.
- [9] O. Senkov, J. Scott, S. Senkova, D. M.-J. of alloys and, and U. 2011, Microstructure and room temperature properties of a high-entropy TaNbHfZrTi alloy, *J. Alloys Compd.* 509 (2011) 6043–6048.
- [10] O.N. Senkov, G. Wilks, J.M. Scott, D.B. Miracle, Mechanical properties of Nb25Mo25Ta25W25 and V20Nb20Mo20Ta20W20 refractory high entropy alloys, *Intermetallics* 19 (2011) 698–706.
- [11] D.G. Kalali, et al., On the origins of ultra-high hardness and strain gradient plasticity in multi-phase nanocrystalline MoNbTaTiW based refractory high-entropy alloy, *Mater. Sci. Eng.* 812 (2021), 141098.
- [12] M. Moorehead, et al., High-throughput synthesis pf Mo-Nb-Ta-W high-entropy alloys via additive manufacturing, *Mater. Des.* 187 (2020), 108358.
- [13] G.C. Gruber, A. Lassnig, S. Zak, C. Gammer, M.J. Cordill, R. Franz, Synthesis and structure of refractory high entropy alloy thin films based on the MoNbTaW system, *Surf. Coat. Technol.* 439 (2022), 128446.
- [14] J.M. Torralba, P. Alvarezdo, A. García-Junceda, High-entropy alloys fabricated via powder metallurgy. A critical review, *Powder Metall.* 62 (2) (2019) 84–114, <https://doi.org/10.1080/00325899.2019.1584454>.

- [15] Z.D. Han, et al., Intermetallics Effect of Ti additions on mechanical properties of NbMoTaW and VNbMoTaW refractory high entropy alloys, *Intermetallics* 84 (2017) 153–157, <https://doi.org/10.1016/j.intermet.2017.01.007>.
- [16] O.N. Senkov, S.V. Senkova, C. Woodward, Effect of aluminum on the microstructure and properties of two refractory high-entropy alloys, *Acta Mater.* 68 (2014) 214–228, <https://doi.org/10.1016/j.actamat.2014.01.029>.
- [17] Z.D. Han, et al., Materials Science & Engineering A Microstructures and Mechanical Properties of Ti X NbMoTaW Refractory High-Entropy Alloys, vol. 712, 2018, pp. 380–385, <https://doi.org/10.1016/j.msea.2017.12.004>. September 2017.
- [18] T. Li, et al., A novel ZrNbMoTaW refractory high-entropy alloy with in-situ forming heterogeneous structure, *Mater. Sci. Eng.* 827 (2021), <https://doi.org/10.1016/j.msea.2021.142061>. June.
- [19] T. Li, Y. Lu, Z. Li, T. Wang, T. Li, *Intermetallics Hot Deformation Behavior and Microstructure Evolution O · Non-equimolar*, vol. 146, 2022. April.
- [20] T. Li, et al., CALPHAD-aided design for superior thermal stability and mechanical behavior in a TiZrHfNb refractory high-entropy alloy, *Acta Mater.* 246 (2023), 118728, <https://doi.org/10.1016/j.actamat.2023.118728>. December 2022.
- [21] T. Li, J. Miao, Y. Lu, T. Wang, T. Li, Effect of Zr on the as-cast microstructure and mechanical properties of lightweight Ti2VNbMoZrx refractory high-entropy alloys, *Int. J. Refracat. Metals Hard Mater.* 103 (2022), <https://doi.org/10.1016/j.ijrmhm.2021.105762>.
- [22] Y. Zou, S. Maiti, W. Steurer, R. Spolenak, Size-dependent plasticity in an Nb25Mo25Ta 25W25 refractory high-entropy alloy, *Acta Mater.* 65 (2014) 85–97, <https://doi.org/10.1016/j.actamat.2013.11.049>. February.
- [23] H. Kim, et al., Mechanical and electrical properties of NbMoTaW refractory high-entropy alloy thin films, *Int. J. Refracat. Metals Hard Mater.* 80 (2019) 286–291, <https://doi.org/10.1016/j.ijrmhm.2019.02.005>. February.
- [24] A. Kanchi, K.V. Rajulapati, B.S. Rao, D. Sivaprasaham, R.C. Gundakaram, Influence of thermomechanical processing on microstructure and mechanical properties of MoNbTaW refractory high-entropy alloy, *J. Mater. Eng. Perform.* (2022), <https://doi.org/10.1007/s11665-022-06855-9>.
- [25] B. Zhang, M.C. Gao, Y. Zhang, S. Yang, S.M. Guo, Senary refractory high entropy alloy MoNbTaTiVW, *Mater. Sci. Technol.* 31 (10) (2015) 1207–1213, <https://doi.org/10.1179/1743284715Y.0000000031>.
- [26] Z.D. Han, et al., Microstructures and mechanical properties of $TixNbMoTaW$ refractory high-entropy alloys, *Mater. Sci. Eng.* 712 (2018) 380–385, <https://doi.org/10.1016/j.msea.2017.12.004>. February 2018.
- [27] Y. Zong, N. Hashimoto, H. Oka, Study on irradiation effects of refractory bcc high-entropy alloy, *Nucl. Mater. Energy* 31 (2022), 101158.
- [28] O.N. Senkov, G. Wilks, D.B. Miracle, C.P. Chunag, P.K. Liaw, Refractory high-entropy alloys, *Intermetallics* 18 (2010) 1758–1765.
- [29] Y. Zou, S. Maiti, W. Steurer, R. Spolenak, Size-dependent plasticity in an Nb25Mo25Ta 25W25 refractory high-entropy alloy, *Acta Mater.* 65 (2014) 85–97.
- [30] X. Wang, P.W. Liu, Y. Ji, Y. Liu, M.H. Horstemeyer, L. Chen, Investigation on Microsegregation of IN178 Alloy during Additive Manufacturing via Integrated Phase-Field and Finite-Element Modeling, vol. 28, 2019, pp. 657–665, <https://doi.org/10.1007/s11665-018-3620-3>. February.
- [31] R.M. Kearsey, *Compositional Effects on Microsegregation Behaviour in Single Crystal Superalloy Systems*, 2004. December.
- [32] W. Zheng, S. Lü, S. Wu, X. Chen, W. Guo, Development of MoNbVTax refractory high entropy alloy with high strength at elevated temperature, *Mater. Sci. Eng.* 850 (2022), 143554, <https://doi.org/10.1016/j.msea.2022.143554>. July.
- [33] C. Lee, et al., Lattice distortion in a strong and ductile refractory high-entropy alloy, *Acta Mater.* 160 (2018) 158–172, <https://doi.org/10.1016/j.actamat.2018.08.053>.
- [34] D. Nath, F. Singh, R. Das, X-ray diffraction analysis by Williamson-Hall, Halder-Wagner and size-strain plot methods of CdSe nanoparticles- a comparative study, *Mater. Chem. Phys.* 239 (2020), 122021, <https://doi.org/10.1016/j.matchemphys.2019.122021>. July 2019.
- [35] V.D. Moté, Y. Purushotham, B.N. Dole, Williamson-Hall Analysis in Estimation of Lattice Strain in Nanometer-Sized ZnO Particles, 2012, pp. 2–9.
- [36] A.M. Montes, XRD Peak Broadening and the Williamson-Hall Analysis, 2014. October.
- [37] N. Singh, Y. Shadangi, V. Shivam, N.K. Mukhopadhyay, MgAlSiCrFeNi low-density high entropy alloy processed by mechanical alloying and spark plasma sintering: effect on phase evolution and thermal stability, *J. Alloys Compd.* 875 (Sep. 2021), 159923, <https://doi.org/10.1016/J.JALLCOM.2021.159923>.
- [38] B.D. Cullity, *Elements of X-Ray Diffraction*, Addison-Wesley Publishing Company, Inc., Reading, MA, 1978.
- [39] H. Bakker, *Enthalpies in Alloys : Miedema's Semi-empirical Model*, Trans Tech publications, Zrich, 1998.
- [40] D. Bagayoko, Understanding density functional theory (DFT) and completing it in practice, *AIP Adv.* 4 (12) (2014), <https://doi.org/10.1063/1.4903408>.
- [41] E. Parthé, Valence-electron concentration rules and diagrams for diamagnetic, non-metallic ionic-covalent compounds with tetrahedrally coordinated anions, *Acta Crystallogr. B* 29 (12) (Dec. 1973) 2808–2815, <https://doi.org/10.1107/S0567740873007570>.
- [42] A. Van De Walle, et al., Efficient stochastic generation of special quasirandom structures, *Calphad Comput. Coupling Phase Diagrams Thermochem.* 42 (2013) 13–18, <https://doi.org/10.1016/j.calphad.2013.06.006>.
- [43] G. Kresse, J. Furthmüller, Efficient iterative schemes for ab initio total-energy calculations using a plane-wave basis set, *Phys. Rev. B* 54 (16) (1996) 11169–11186, <https://doi.org/10.1103/PhysRevB.54.11169>.
- [44] P.E. Blöchl, Projector augmented-wave method, *Phys. Rev. B* 50 (24) (1994) 17953–17979, <https://doi.org/10.1103/PhysRevB.50.17953>.
- [45] J.P. Perdew, K. Burke, M. Ernzerhof, Generalized gradient approximation made simple, *Phys. Rev. Lett.* 77 (18) (1996) 3865–3868, <https://doi.org/10.1103/PhysRevLett.77.3865>.
- [46] V. Wang, N. Xu, J.C. Liu, G. Tang, W.T. Geng, VASPKIT: a user-friendly interface facilitating high-throughput computing and analysis using VASP code, *Comput. Phys. Commun.* 267 (2021), 108033, <https://doi.org/10.1016/j.cpc.2021.108033>.
- [47] N.K. Mukhopadhyay, P. Paufler, Micro- and nanoindentation techniques for mechanical characterisation of materials, *Int. Mater. Rev.* 51 (4) (2006) 209–245, <https://doi.org/10.1179/174328006X102475>.
- [48] M. Vaidya, G. Muralikrishna, B. Murty, High-entropy alloys by mechanical alloying: a review, *J. Mater. Res.* (2019) 664–686, <https://doi.org/10.1557/jmr.2019.37>.
- [49] N.K. Mukhopadhyay, Meeting report: high entropy alloys: a renaissance in physical metallurgy, *Curr. Sci.* 109 (4) (2015) 665–667.
- [50] W. Steurer, Single-phase high-entropy alloys - a critical update, *Mater. Char.* 162 (2020), 110179, <https://doi.org/10.1016/j.colsurfa.2020.124658>.
- [51] A.R. Miedema, F.R. de Boer, R. Boom, Model predictions for the enthalpy of formation of transition metal alloys, *Calphad* 1 (4) (1977) 341–359, [https://doi.org/10.1016/0364-5916\(77\)90011-6](https://doi.org/10.1016/0364-5916(77)90011-6).
- [52] A.R. Miedema, F.R. De Boer, R. Boom, Predicting heat effects in alloys, *Phys. B+C* 103 (1) (1981) 67–81, [https://doi.org/10.1016/0378-4363\(81\)90032-2](https://doi.org/10.1016/0378-4363(81)90032-2).
- [53] X. Yang, Y. Zhang, Prediction of high-entropy stabilized solid-solution in multi-component alloys, *Mater. Chem. Phys.* 132 (2–3) (2012) 233–238, <https://doi.org/10.1016/j.matchemphys.2011.11.021>.
- [54] S. Guo, C. Ng, J. Lu, C.T. Liu, Effect of valence electron concentration on stability of fcc or bcc phase in high entropy alloys, *J. Appl. Phys.* 109 (10) (2011), <https://doi.org/10.1063/1.3587228>.
- [55] N. Singh, Y. Shadangi, N.K. Mukhopadhyay, Phase evolution and thermal stability of low-density MgAlSiCrFe high-entropy alloy processed through mechanical alloying, *Trans. Indian Inst. Met.* 73 (2020) 2377–2386, <https://doi.org/10.1007/s12666-020-02039-y>.
- [56] N. Singh, Y. Shadangi, G.S. Goud, V.K. Pandey, V. Shivam, N.K. Mukhopadhyay, Fabrication of MgAlSiCrFe low-density high-entropy alloy by mechanical alloying and spark plasma sintering, *Trans. Indian Inst. Met.* 74 (9) (2021) 2203–2219, <https://doi.org/10.1007/s12666-021-02262-1>.
- [57] V. Shivam, J. Basu, Y. Shadangi, M.K. Singh, N.K. Mukhopadhyay, Mechanico-chemical synthesis, thermal stability and phase evolution in AlCoCrFeNi high entropy alloy, *J. Alloys Compd.* 757 (2018) 87–97, <https://doi.org/10.1016/j.jallcom.2018.05.057>.
- [58] V.K. Pandey, et al., Synthesis, characterization and thermal stability of nanocrystalline MgAlMnFeCu low-density high-entropy alloy, *Trans. Indian Inst. Met.* 74 (1) (2021) 33–44, <https://doi.org/10.1007/s12666-020-02114-4>.
- [59] V. Shivam, J. Basu, V.K. Pandey, Y. Shadangi, N.K. Mukhopadhyay, Alloying behaviour, thermal stability and phase evolution in quinary AlCoCrFeNi high entropy alloy, *Adv. Powder Technol.* 29 (9) (2018) 2221–2230, <https://doi.org/10.1016/j.japt.2018.06.006>.
- [60] Y.L. Chen, Y.H. Hu, C.A. Hsieh, J.W. Yeh, S.K. Chen, Competition between elements during mechanical alloying in an octenary multi-principal-element alloy system, *J. Alloys Compd.* 481 (1–2) (2009) 768–775, <https://doi.org/10.1016/j.jallcom.2009.03.087>.
- [61] J. Han, B. Su, J. Lu, J. Meng, A. Zhang, Y. Wu, Preparation of MoNbTaW refractory high entropy alloy powders by pressureless spark plasma sintering: crystal structure and phase evolution, *Intermetallics* 123 (2020), 106832.
- [62] V. Laxmanan, ANALYSIS OF CURRENT THEORIES AND MODELS 33 (6) (1985).
- [63] H.W. Yao, J.W. Qiao, J.A. Hawk, H.F. Zhou, M.W. Chen, M.C. Gao, Mechanical properties of refractory high-entropy alloys : experiments and modeling, *J. Alloys Compd.* 696 (2017) 1139–1150, <https://doi.org/10.1016/j.jallcom.2016.11.188>.
- [64] H.W. Yao, et al., NbTaV-(Ti,W) refractory high-entropy alloys: experiments and modeling, *Mater. Sci. Eng.* 674 (2016) 203–211, <https://doi.org/10.1016/j.msea.2016.07.102>.
- [65] H.W. Yao, et al., Materials Science & Engineering A NbTaV- (Ti , W) Refractory High-Entropy Alloys : Experiments and Modeling Mole Fraction Mole Fraction Temperature [K] Mole Fraction Temperature [K], vol. 674, 2016, pp. 203–211, <https://doi.org/10.1016/j.msea.2016.07.102>.
- [66] D.H. Chung, W.R. Buessem, The VoigtReussHill (VRH) approximation and the elastic moduli of polycrystalline ZnO, TiO₂ (rutile), and Al₂O₃ the voigt-reuss-hill (VRH) approximation and the elastic Moduli of Polycrystalline 2 (1968) 2013, <https://doi.org/10.1063/1.1656672>.
- [67] D.-H. Chung, Elastic moduli of single crystal and polycrystalline MgO, *Philos. Mag. A J. Theor. Exp. Appl. Phys.* 8 (89) (1963) 833–841, <https://doi.org/10.1080/14786436308213840>.
- [68] Berechnung der Fließgrenze von Mischkristallen auf Grund der Plastizitätsbedingung für Einkristalle, vol. 8. 1928.
- [69] D.G. Pettifor, Theoretical predictions of structure and related properties of intermetallics, *Mater. Sci. Technol.* 8 (4) (Apr. 1992) 345–349, <https://doi.org/10.1179/mst.1992.8.4.345>.
- [70] D. Tabor, The hardness of solids, *Rev. Phys. Technol.* 1 (3) (Jan. 1970) 145–179, <https://doi.org/10.1088/0034-6683/1/3/011>.
- [71] L. Raman, et al., Strengthening mechanisms in CrMoNbTiW refractory high entropy alloy, *Mater. Sci. Eng.* 819 (2021), <https://doi.org/10.1016/j.msea.2021.141503>. March.
- [72] K. Balasubramanian, S.V. Khare, D. Gall, Valence electron concentration as an indicator for mechanical properties in rocksalt structure nitrides, carbides and carbonitrides, *Acta Mater.* 152 (2018) 175–185, <https://doi.org/10.1016/j.actamat.2018.04.033>.